CARBON 82 (2015) 572–578

Available at www.sciencedirect.com

ScienceDirect

journal homepage: www.elsevier.com/locate/carbon

Yolk–shell structured iron carbide/N-doped carbon composite as highly efficient and stable oxygen reduction reaction electrocatalyst

Lingzheng Gu [a,b], *Luhua Jiang* [a,*], *Jutao Jin* [a], *Jing Liu* [a,b], *Gongquan Sun* [a,*]

[a] *Fuel Cell & Battery Division, Dalian National Laboratory for Clean Energy, Dalian Institute of Chemical Physics, Chinese Academy of Sciences, Dalian 116023, China*

[b] *University of Chinese Academy of Sciences, Beijing 100039, China*

ARTICLE INFO

Article history:
Received 5 September 2014
Accepted 3 November 2014
Available online 8 November 2014

ABSTRACT

We report a simple route to synthesize iron carbide/carbon yolk–shell composite via a facile two-step process including polymerization of pyrrole using Fe_3O_4 as a sacrificial template to form a Fe_3O_4/polypyrrole composite, followed by annealing at high temperature in N_2 atmosphere. The yolk–shell composite, with iron carbide ($Fe_{2.5}C$) embedded in nitrogen-doped carbon layers, shows impressively high catalytic activity and stability for oxygen reduction reaction in alkaline solution. Both the pyridinic-N and graphic-N in the shell of Fe_3O_4–PPy-700, together with the $Fe_{2.5}C$ confined in carbon layers are believed to be the active sites for the ORR.

1. Introduction

One of the major challenges for development of fuel cells is the sluggish kinetics of the oxygen reduction reaction (ORR) at the cathode. Pt-based metals are considered as the most active electrocatalysts towards the ORR; however, the high cost and scarce reserve of platinum limit its extensive use practically. Thus, designing alternative ORR electrocatalysts with high catalytic performance and low cost to supersede Pt is of great interests [1].

Among the non-precious metal electrocatalysts investigated, carbon materials doped with heteroatom, such as N, B, S, etc., have attracted great attention due to their promising catalytic performance towards the ORR [2–4]. Despite the ongoing debates on the catalytic center, nitrogen incorporated into carbon matrix in graphitic or pyridinic form is deemed to be crucial for the ORR [2,5]. Recently, metal or metal carbides buried under carbon layers with core–shell structures [6,7] or pod-like structures [8], have been reported active and stable as the ORR electrocatalysts by virtue of the protective outer graphitic layers. More recently, Xing and co-workers have reported Fe_3C encased by graphitic layers (Fe_3C/C) to be an active and stable electrocatalyst for the ORR and the Fe_3C phase is demonstrated to play a key role in promoting the ORR. It is also reported that N-doped ketjen-black and Fe/Fe_3C of melamine carbon foam [9] or Fe/Fe_3C nanoparticles encapsulated in nitrogen-doped carbon [10] were responsible for the ORR activity. Therefore, it is promising to fabricate a hybrid material composed of both nitrogen-doped carbon and Fe_3C nanoparticles enveloped within the graphitic layers as the electrocatalysts for the ORR.

Here, we developed a novel self-sacrificial template route to synthesize an iron carbide/N-doped carbon composite with a yolk–shell structure, in which the outer shell is composed of nitrogen-doped carbon enveloping ultrafine iron carbide particles, while the inner yolk is composed of iron carbide. The

* *Corresponding authors:* Fax: +86 041184379063.
E-mail addresses: sunshine@dicp.ac.cn (L. Jiang), gqsun@dicp.ac.cn (G. Sun).

http://dx.doi.org/10.1016/j.carbon.2014.11.010
0008-6223/

composite shows excellent activity and stability for the ORR in alkaline electrolyte.

2. Experimental

2.1. Synthesis of Fe_3O_4–PPy, Fe_3O_4–PPy-700 and PPy-700

The synthesis procedure of Fe_3O_4–PPy-700 is displayed in Fig. 1. Firstly, 300 mg of Fe_3O_4 powder (100–300 nm Aladdin Industrial Corporation, Shanghai, China) was added into 70 mL of deionized water and stirred for 15 min to form a suspension. Subsequently, 3 mL of pyrrole (Sinopharm Chemical Reagent Co., Ltd.) dispersed in 15 mL of ethanol was added into the above suspension and stirred ultrasonically for 20 min. After that, 15 mL of HCl aqueous solution (6 M) was added into the above suspension and sonicated for 1.5 h. In fact, once the HCl solution was added, the Fe_3O_4 nanoparticles began to be eroded and released Fe^{3+} ions slowly. These Fe^{3+} ions initiated the polymerization of pyrrole into polypyrrole (PPy) around the remaining Fe_3O_4 nanoparticles [11]. During this process, the Fe_3O_4 nanoparticles became smaller and enwrapped by polypyrrole gradually. The product was filtered to obtain a black cake, which was then dispersed in 70 mL of 0.5 M H_2SO_4 aqueous solution under sonication for 4 h to allow the exposed iron oxides leached out. The black suspension was filtered, washed and dried to obtain black product, which was labeled as Fe_3O_4–PPy. The Fe_3O_4–PPy was then thermally annealed at 700 °C in N_2 for 30 min to obtain the finally catalyst, which was labeled as Fe_3O_4–PPy-700.

For comparison, PPy without iron was pyrolized to obtain nitrogen-doping carbon. The preparation procedure is as follow. First, 4.2 g of $(NH_4)_2S_2O_8$ (Tianjin Damao Reagent Factory) was dissolved in 80 mL deionized water under the constant stirring. Then, 1.2 mL of pyrrole was added into the solution. After that, the mixture was stirred continuously for 4 h and the mixture was gradually turned black. The black suspension was filtered, washed, dried and finally pyrolized as the same procedure of Fe_3O_4–PPy-700. The final catalyst was labeled as PPy-700.

2.2. Physical characterization

The morphology of Fe_3O_4–PPy-700 was investigated using ultra-high resolution scanning electron microscope (HR-SEM) and high resolution transmission electron microscopy (HRTEM). The HR-SEM and HRTEM images were obtained using Hitachi S-5500 and Tecnai G2 F30 S-Twin (FEI, accelerated voltage: 300 kV), respectively. The crystal structures of Fe_3O_4–PPy and Fe_3O_4–PPy-700 were investigated by X-ray diffraction (XRD) technique on a Rigaku X-2000 diffractometer using Cu Kα radiation with a Ni filter. The samples were scanned from 5° to 85° (2θ) at the scan rate of 5° min^{-1}. The chemical compositions of Fe_3O_4–PPy and Fe_3O_4–PPy-700 were characterized with X-ray photoelectron spectroscopy (XPS) measurements (ESCALAB 250Xi) with X ray sources of Al K_α.

2.3. Electrochemical measurements

Rotating ring disc electrode (RRDE) measurements were conducted in a three-electrode cell setup with a computer-controlled bipotentiostat (Pine Company). The reference electrode was Hg/HgO electrode (MMO) in 0.1 M NaOH solution, and the counter electrode was Pt wire. The MMO reference electrode was calibrated and the potential was converted into reversible hydrogen electrode (RHE) in this paper. To prepare the working electrode, 2.5 mg of catalyst powder was dispersed in 1 mL of ethanol and 30 μL of Nafion® solution (5 wt%, DuPont), which was sonicated for 15 min to form homogeneous ink, and then, 52 μL of the ink was pipetted on the surface of the glassy carbon disc (Ø5.7 mm) to form a catalyst loading of 0.49 mg cm^{-2}. The working electrode surface was first electrochemically cleaned by cycling from 0.11 to 1.23 V (vs. RHE) for 20 cycles with a scanning rate of 100 mV s^{-1}, and then the background cyclic voltammogram (CV) was first collected at a scan rate of 10 mV s^{-1} in N_2-saturated 0.1 M NaOH electrolyte. Then the RRDE measurement was carried out in O_2-saturated 0.1 M NaOH electrolyte at a scanning rate of 10 mV s^{-1}. The collection efficiency (N) for H_2O_2 by the RRDE is 0.38 [12]. The potential

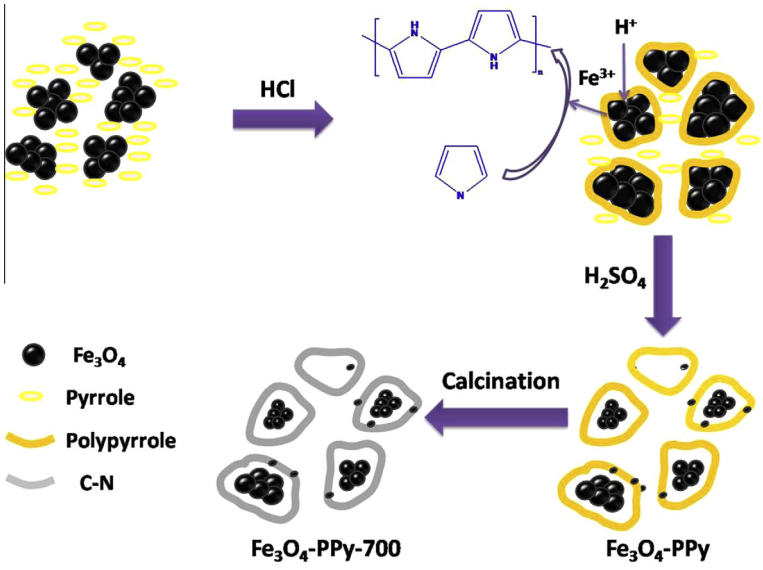

Fig. 1 – Synthesis procedure of Fe_3O_4–PPy and Fe_3O_4–PPy-700. (A color version of this figure can be viewed online.)

applied to the ring electrode was held at 1.23 V (vs. RHE). The methanol tolerance experiment was tested in 0.1 M NaOH electrolyte plus 0.1 M MeOH. The accelerated aging test was carried out in O_2-saturated 0.1 M NaOH electrolyte scanning in the range of 0.60–1.00 V (vs. RHE) with the scan rate of 100 mV s^{-1}. The background CVs and the ORR polarization curves were recorded every 1000 potential cycles during the accelerated aging test.

3. Results and discussion

3.1. *Physical characterization of Fe_3O_4–PPy and Fe_3O_4–PPy-700*

The morphology and microstructure of Fe_3O_4–PPy-700 characterized by HR-SEM, HRTEM and XRD are shown in Fig. 2. As observed in the SEM image in Fig. 2a, the Fe_3O_4–PPy-700 composite is composed of large spheres of around 400–500 nm in diameter. From the HAADF-STEM image in Fig. 2b and the TEM image in Fig. 2c, it can be seen clearly that most of the spheres are of yolk–shell structure, with a shell of about 30–40 nm in thickness enveloping a yolk of about 140 nm. A closer observation of the microstructure of the composite in the HRTEM image as shown in Fig. 2d, shows clearly the crystal lattice fringes of about 0.273 nm, which corresponds to the lattice distance for the $CFe_{2.5}$ (3,1,−1) planes, suggesting the yolk is composed of $CFe_{2.5}$. Further closer observation on the shell of the composite as shown in Fig. 2e confirms that it is composed of ultrafine nanoparticles (<15 nm), most of which might be amorphous carbon and a few dark particles embedded in thin carbon layers which are deduced to be $CFe_{2.5}$ and Fe particles according to the spacing of crystalline

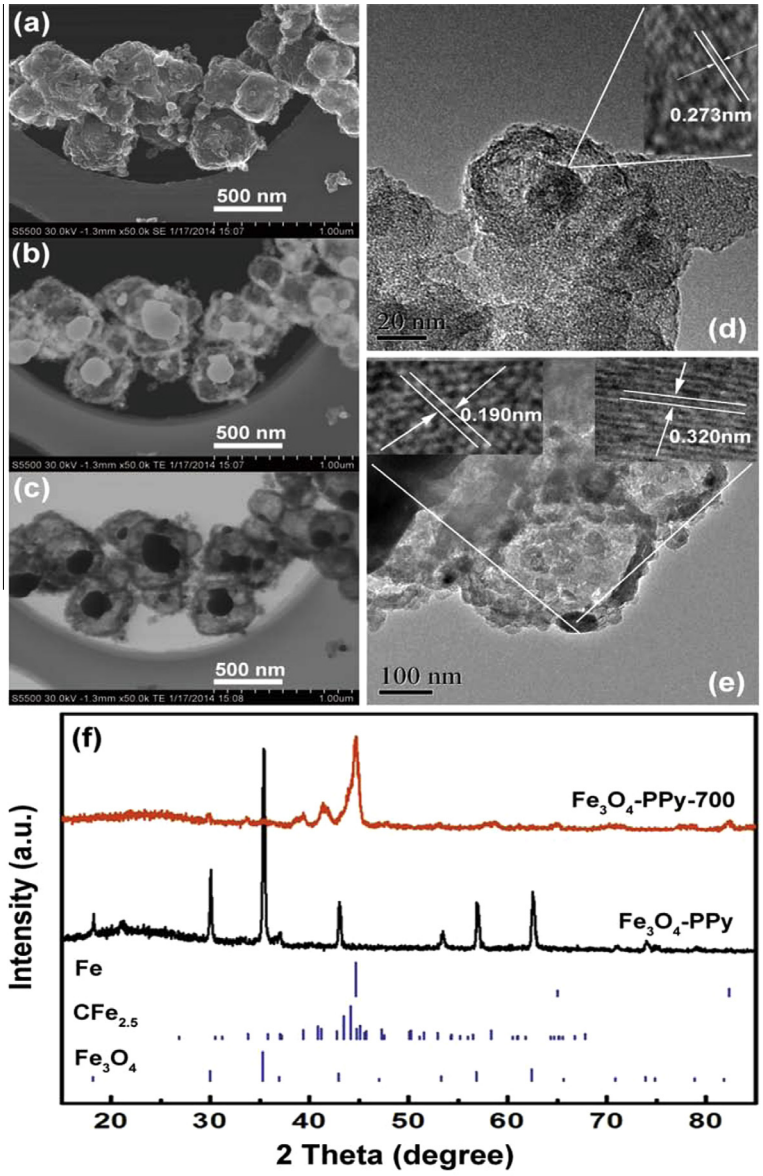

Fig. 2 – (a) SEM, (b) HAADF-TEM, (c) TEM and (d and e) HRTEM images of Fe_3O_4–PPy-700. (f) XRD patterns of Fe_3O_4–PPy-700 and Fe_3O_4–PPy. The inset of d and e show the magnified TEM images of the yolk and the shell of Fe_3O_4–PPy-700, respectively. (A color version of this figure can be viewed online.)

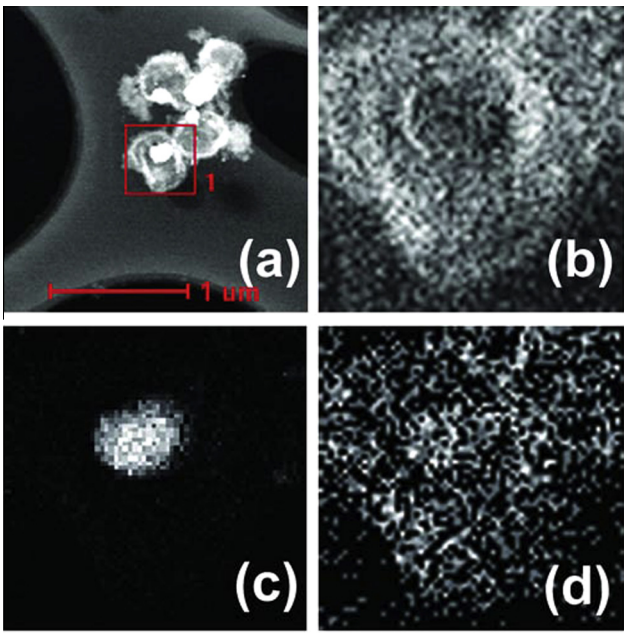

Fig. 3 – (a) HRTEM image of Fe_3O_4–PPy-700 and elemental mappings of (b) carbon, (c) iron, (d) nitrogen in Fe_3O_4–PPy-700. (A color version of this figure can be viewed online.)

lattices of 0.320 nm corresponding to $CFe_{2.5}$ (11-1) planes and 0.190 nm corresponding to Fe (110) planes. The X-ray diffraction (XRD) patterns of the Fe_3O_4–PPy and Fe_3O_4–PPy-700 composites are shown in Fig. 2f. For clear comparison, the standard diffraction patterns of metallic iron (JCPDS 65-4899), $CFe_{2.5}$ (JCPDS 36-1248) and Fe_3O_4 (JCPDS 65-3107) are also displayed in Fig. 2f. For the Fe_3O_4–PPy, the diffraction peaks locating at near 35.5°, 30.1° and 43.1° are consistent with those for Fe_3O_4. For the Fe_3O_4–PPy-700, the diffraction peaks locating at 44.2°, 43.5° and 82.3° are consistent with those for $CFe_{2.5}$ and the diffraction peaks at 44.7°, 33.8° and 26.8° are from metallic iron, indicating the co-existence of $CFe_{2.5}$ and Fe. This is consistent with the TEM analysis. Additionally, the XRD results confirm that the remaining Fe_3O_4 in Fe_3O_4–PPy composite completely transformed into $CFe_{2.5}$ and metallic iron after annealed at 700 °C.

The chemical composition of the Fe_3O_4–PPy-700 is analyzed by EDX equipped on HRTEM. In the HRTEM image shown in Fig. 3a, single yolk–shell composite was selected randomly for elemental analysis. Fig. 3b–d represents the local distributions of carbon, iron, and nitrogen, respectively, in the composite. As shown in Fig. 3b and d, the distribution of carbon is almost overlapped with nitrogen and both are uniformly distributed. While for iron, except for the extensive distribution in the core of the composite, iron is also detected in the shells and distributes uniformly.

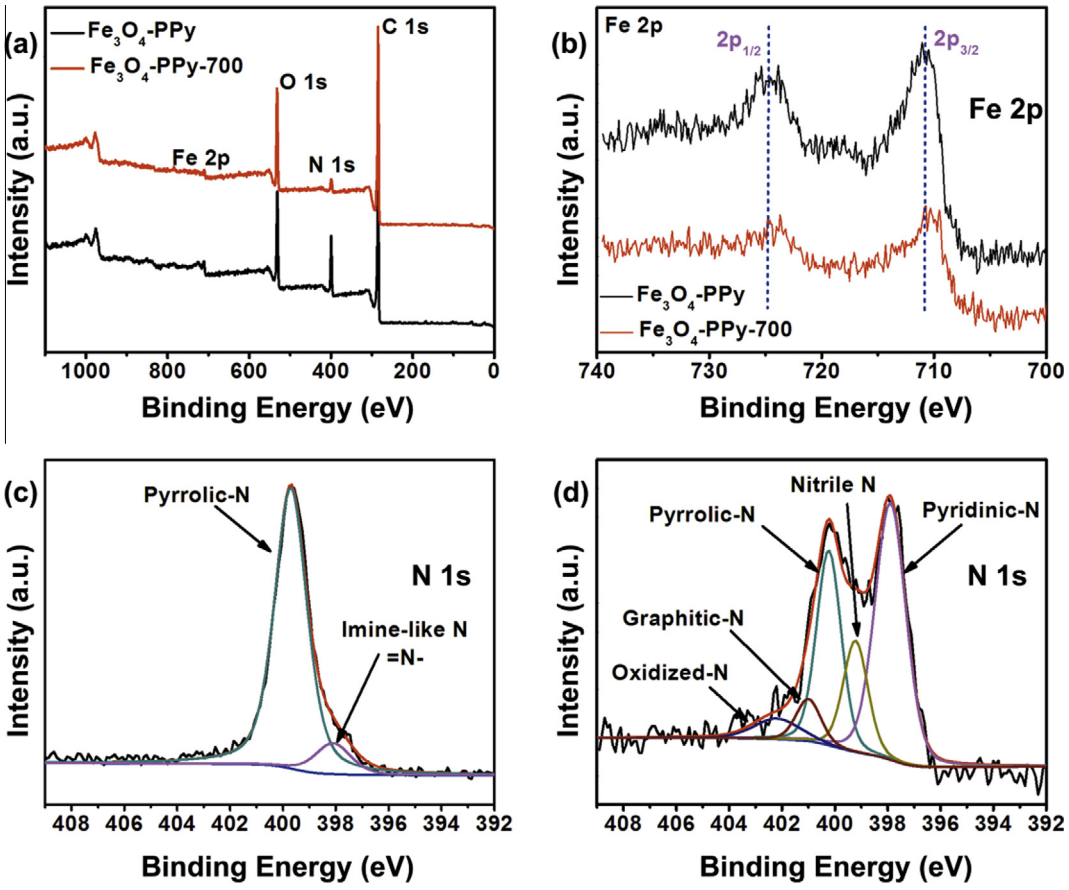

Fig. 4 – (a) Sum XPS spectra for Fe_3O_4–PPy and Fe_3O_4–PPy-700. XPS spectra of (b) Fe 2p for Fe_3O_4–PPy and Fe_3O_4–PPy-700, (c) N 1s for Fe_3O_4–PPy and (d) N 1s for Fe_3O_4–PPy-700. (A color version of this figure can be viewed online.)

Table 1 – Elemental composition (at.%) of Fe_3O_4–PPy and Fe_3O_4–PPy-700.

Elemental composition	C 1s	N 1s	O 1s	Fe 2p
Fe_3O_4–PPy	68.84	13.13	17.04	0.99
Fe_3O_4–PPy-700	78.66	3.61	17.24	0.5

Table 2 – Contents of different types of N in Fe_3O_4–PPy-700 and Fe_3O_4–PPy.

		Pyridinic-N	Nitrile-N	Pyrrolic-N	Graphitic-N	Oxidized-N	Imine-like N
Fe_3O_4–PPy-700	B.E. (eV)	397.9	399.2	400.2	401	402.2	–
	at.%	45	16	28	6	5	–
Fe_3O_4–PPy	B.E. (eV)	–	–	399.7	–	–	398.1
	at.%	–	–	90	–	–	10

3.2. *Chemical and structural analysis*

The surface elemental compositions of Fe_3O_4–PPy and Fe_3O_4–PPy-700 are analyzed from the XPS spectra. As shown in Fig. 4a, the peaks centered at 284, 398, 532 and 710 eV correspond to C 1s, N 1s, O 1s and Fe 2p, respectively. The elemental compositions in atomic ratios for both composites are listed in Table 1. It is noted that the content of nitrogen in Fe_3O_4–PPy is higher than in Fe_3O_4–PPy-700, which is reasonable considering that partial PPy might decompose during the thermal treatment. The Fe 2 p spectra for both samples are displayed in Fig. 4b. For Fe_3O_4–PPy, the peaks at 724.7 and 710.8 eV, are assigned to Fe $2p_{1/2}$ and Fe $2p_{3/2}$ of Fe_3O_4 [13,14]. Compared with Fe_3O_4–PPy, the peaks of Fe $2p_{1/2}$ and Fe $2p_{3/2}$ for Fe_3O_4–PPy-700 shifted to the lower binding energy, which indicates that Fe_3O_4 in Fe_3O_4–PPy was reduced during the calcination. The previous XRD results also provide evidence that the Fe_3O_4 in Fe_3O_4–PPy is reduced into $CFe_{2.5}$ and Fe in the Fe_3O_4–PPy-700 composite. The N 1s spectra for Fe_3O_4–PPy and Fe_3O_4–PPy-700 are depicted in Fig. 4c and d, respectively. For Fe_3O_4–PPy, the N 1s spectrum can be deconvoluted into two peaks, at around 399.7 and 398.1 eV, corresponding to pyrrole-N [3] and imine-like N (=N–) [15], respectively. While for Fe_3O_4–PPy-700, the N 1s spectrum can be deconvoluted into five peaks at around 402.2, 401.0, 400.2, 399.2 and 397.9 eV, corresponding to pyridinic-N, nitrile-N, pyrrolic-N, graphitic-N and oxidized-N [16], respectively. By integrating the peak areas, the relative content of N is calculated and listed in Table 2. For the Fe_3O_4–PPy, pyrrole-N is dominant (90 at.%), supporting the presence of PPy in the Fe_3O_4–PPy composite. The contents for pyridinic-N, nitrile-N, pyrrolic-N, graphitic-N and oxidized-N in the Fe_3O_4–PPy-700 composite are 45, 16, 28, 6 and 5 at.%, respectively. It is apparent that although the total content of nitrogen in Fe_3O_4–PPy-700 decreases, as compared with Fe_3O_4–PPy, the N in forms of pyridinic-N and graphic-N are generated after annealing, which are believed to be active for the ORR [2,5,17].

3.3. *Activity and stability towards ORR*

The electrocatalytic activity and selectivity of Fe_3O_4–PPy, Fe_3O_4–PPy-700 and PPy-700 for the ORR were examined in

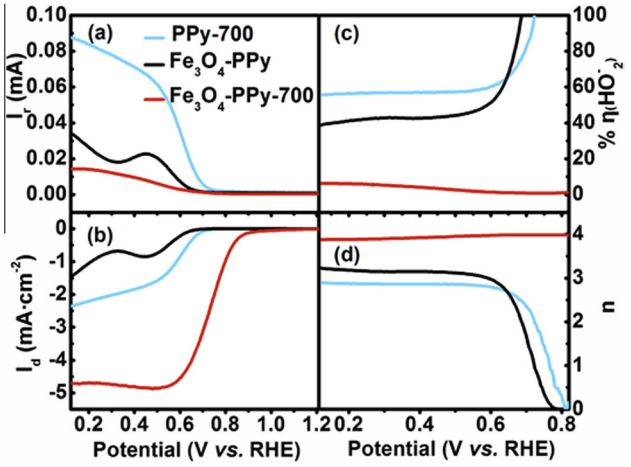

Fig. 5 – Oxygen reduction reaction measurements of PPy-700, Fe_3O_4–PPy and Fe_3O_4–PPy-700 on RRDE. (a) Ring currents, (b) disc currents, (c) HO_2^- yield, and (d) electron-transfer numbers. Rotation rate: 1600 rpm; scan rate: 10 mV s^{-1}. (A color version of this figure can be viewed online.)

0.1 M NaOH solution saturated with oxygen by RRDE technique with the rotating rate of 1600 rpm. The ring and disc currents are plotted in Fig. 5a and b, respectively. According to the ORR polarization curves for both samples in Fig. 5b, both the onset potential (E_0) and the half-wave potential ($E_{1/2}$) of the ORR curve with Fe_3O_4–PPy-700 as the catalyst are significantly positive than those with Fe_3O_4–PPy and PPy-700. The ORR limiting current density for Fe_3O_4–PPy-700 approaches to 5 mA cm^{-2}, while for Fe_3O_4–PPy and PPy-700, it is only about 1.5 and 2.5 mA/cm^2, respectively. The yield of HO_2^- (η) and the electron transfer number (n) calculated according to Eqs. (1) and (2) are also plotted in Fig. 5c and d, respectively.

$$\eta = \frac{200 \times I_r}{N \times I_d + I_r} \quad (1)$$

$$n = \frac{4 \times I_d}{I_d + I_r/N} \quad (2)$$

where I_r is the ring current, I_d the disc current, and N the collection efficiency ($N = 0.38$).

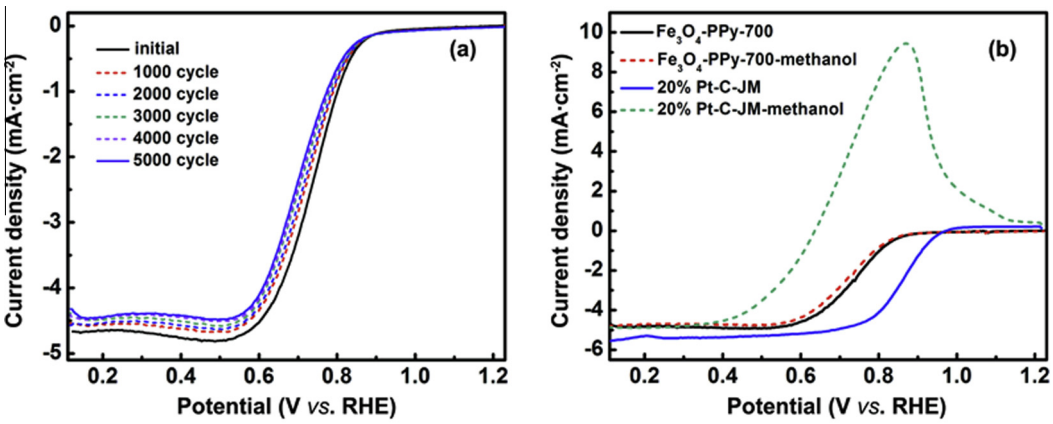

Fig. 6 – (a) ORR polarization plots of Fe_3O_4–PPy-700 electrocatalysts measured during 5000 cycles durability in O_2-saturated 0.1 M NaOH. (b) Linear down sweep potential scan curves of Fe_3O_4–PPy-700 and 20 wt% Pt-JM electrocatalysts obtained with a rotating speed of 1600 rpm for the ORR in O_2-saturated 0.1 M NOH containing 0.1 M methanol. (A color version of this figure can be viewed online.)

It can been seen that the yield of HO_2^- is no more than 6% and the ORR electron transfer number is no less than 3.85 for Fe_3O_4–PPy-700 in the potential window of 0.12–0.81 V (vs. RHE). While for Fe_3O_4–PPy and PPy-700, the electron transfer number is only near 3 in the potential window of 0.12–0.60 V (vs. RHE), which then decreases sharply to almost zero as the potential is positive than 0.60 V (vs. RHE), suggesting 2-electron pathway is dominant for these two catalysts. It is reasonable that the apparent electron-transfer number is higher than 2 if considering the re-adsorption and re-reduction of H_2O_2 in the porous carbon electrode as discussed in our previous paper [12,18]. Additionally, the higher H_2O_2 production together with the higher ORR current for the PPy-700 than those for the Fe_3O_4–PPy also indicates a 2-electron dominant pathway.

The stability of Fe_3O_4–PPy-700 was tested by the accelerated aging method (see experimental). As shown in Fig. 6 a, after 1000 cycles, the half-wave potential $E_{1/2}$ of the ORR shifts negatively about 15 mV and from 1000 to 5000 cycles, $E_{1/2}$ shifts negatively about only 27 mV, indicating a good stability of this catalyst.

Considering methanol is a well known potential poison for cathodic ORR catalyst in a direct methanol fuel cell. Fe_3O_4–PPy-700 was also evaluated by RDE in O_2-saturated 0.1 M NaOH electrolyte containing 0.1 M methanol and the curves are depicted in Fig. 6b. The commercial Pt/C catalyst (20% Pt, denoted as 20% Pt–C-JM) is used for comparison. It can be seen that Fe_3O_4–PPy-700 shows superior tolerance against methanol since the ORR polarization curve keeps almost unchanged in methanol containing electrolyte (dashed line), compared to the methanol-free ORR curve, in contrast, 20% Pt–C-JM shows a significant methanol oxidation current, so that the ORR polarization curve is distorted severely.

The superior activity and durability of the Fe_3O_4–PPy-700 could be related with the special yolk–shell structure composed of nitrogen-doped carbon shell and the subsurface $Fe_{2.5}C$ confined in carbon layers. With such a structure, except for the considerable amount of pyridinic-N and graphic-N in the carbon shell which are believed to be the active sites for the ORR [2,5,17], the $Fe_{2.5}C$ confined in carbon layers may also contribute to the ORR activity. Considering the fact that the carbon shell wrapped outside of $Fe_{2.5}C$ nanoparticle is porous, oxygen molecules could possible penetrate into the core and thus the $Fe_{2.5}C$ yolk might also play role to catalyze the ORR.

4. Conclusions

A yolk–shell structured $Fe_{2.5}C$/nitrogen-doped composite Fe_3O_4–PPy-700 was synthesized by a simple route, in which Fe_3O_4 was employed as a sacrificial template, followed by leaching exposed Fe_3O_4 in H_2SO_4 solution and subsequently annealed at high temperature in N_2 atmosphere. The shell of the Fe_3O_4–PPy-700 composite is composed of nitrogen-doped carbon and $Fe_{2.5}C$ confined in carbon layers, and the yolk contains $Fe_{2.5}C$. The special yolk–shell structured Fe_3O_4–PPy-700 endows highly efficient ORR activity and stability in alkaline media. Both the pyridinic-N and graphic-N in the shell of Fe_3O_4–PPy-700, together with the $Fe_{2.5}C$ confined in carbon layers are believed to be the active site for the ORR. This work is expected to provide new clues to synthesize efficient ORR electrocatalysts of multi-active centers.

Acknowledgements

This work was financially supported by the “Strategic Priority Research Program” of the Chinese Academy of Sciences (XDA09030104), the National Basic Research Program of China (2012CB215500) and Natural Science Foundation of China (20973169).

REFERENCES

[1] Dodelet J-P. Oxygen reduction in PEM fuel cell conditions: heat-treated non-precious metal-N4 macrocycles and beyond. In: Zagal J, Bedioui F, Dodelet J-P, editors. N4-macrocyclic metal complexes. New York: Springer; 2006. p. 83–147.

[2] Li X, Popov BN, Kawahara T, Yanagi H. Non-precious metal catalysts synthesized from precursors of carbon, nitrogen,

and transition metal for oxygen reduction in alkaline fuel cells. J Power Sources 2011;196(4):1717–22.
[3] Yang L, Jiang S, Zhao Y, Zhu L, Chen S, Wang X, et al. Boron-doped carbon nanotubes as metal-free electrocatalysts for the oxygen reduction reaction. Angew Chem Int Ed 2011:7132–5.
[4] Yang Z, Yao Z, Li G, Fang G, Nie H, Liu Z, et al. Sulfur-doped graphene as an efficient metal-free cathode catalyst for oxygen reduction. ACS Nano 2011;6(1):205–11.
[5] Li X, Liu G, Popov BN. Activity and stability of non-precious metal catalysts for oxygen reduction in acid and alkaline electrolytes. J Power Sources 2010;195(19):6373–8.
[6] Chung HT, Won JH, Zelenay P. Active and stable carbon nanotube/nanoparticle composite electrocatalyst for oxygen reduction. Nat Commun 2013:4.
[7] Wen Z, Ci S, Zhang F, Feng X, Cui S, Mao S, et al. Nitrogen-enriched core–shell structured Fe/Fe_3C-C nanorods as advanced electrocatalysts for oxygen reduction reaction. Adv Mater 2012;24(11):1399–404.
[8] Deng D, Yu L, Chen X, Wang G, Jin L, Pan X, et al. Iron encapsulated within pod-like carbon nanotubes for oxygen reduction reaction. Angew Chem Int Ed 2012: 371–5.
[9] Lee J-S, Park GS, Kim ST, Liu M, Cho J. A highly efficient electrocatalyst for the oxygen reduction reaction: N-doped ketjenblack incorporated into Fe/Fe_3C-functionalized melamine foam. Angew Chem 2013;125(3):1060–4.
[10] Wang J, Wang G, Miao S, Jiang X, Li J, Bao X. Synthesis of Fe/Fe_3C nanoparticles encapsulated in nitrogen-doped carbon with single-source molecular precursor for the oxygen reduction reaction. Carbon 2014;75:381–9.
[11] Wang Y, Zou B, Gao T, Wu X, Lou S, Zhou S. Synthesis of orange-like Fe_3O_4/PPy composite microspheres and their excellent Cr(VI) ion removal properties. J Mater Chem 2012;22(18):9034–40.
[12] Liu J, Jiang L, Tang Q, Zhang B, Su DS, Wang S, et al. Coupling effect between cobalt oxides and carbon for oxygen reduction reaction. ChemSusChem 2012;5(12):2315–8.
[13] Ye Y, Kuai L, Geng B. A template-free route to a Fe_3O_4–Co_3O_4 yolk–shell nanostructure as a noble-metal free electrocatalyst for ORR in alkaline media. J Mater Chem 2012;22(36):19132–8.
[14] Li X, Huang X, Liu D, Wang X, Song S, Zhou L, et al. Synthesis of 3D hierarchical Fe_3O_4/graphene composites with high lithium storage capacity and for controlled drug delivery. J Phys Chem C 2011;115(44):21567–73.
[15] Nam D-H, Kim M-J, Lim S-J, Song I-S, Kwon H-S. Single-step synthesis of polypyrrole nanowires by cathodic electropolymerization. J Mater Chem A 2013;1(27):8061–8.
[16] Jaouen F, Herranz J, Lefevre M, Dodelet J-P, Kramm UI, Herrmann I, et al. Cross-laboratory experimental study of non-noble-metal electrocatalysts for the oxygen reduction reaction. ACS Appl Mater Interfaces 2009;1(8):1623–39.
[17] Wang Y, Cui X, Li Y, Chen L, Chen H, Zhang L, et al. A co-pyrolysis route to synthesize nitrogen doped multiwall carbon nanotubes for oxygen reduction reaction. Carbon 2014;68:232–9.
[18] Jiang L, Tang Q, Sun G. Chin J Catal 2014 [accept].